

Noise reduction mechanism of airfoils with leading-edge serrations and surface ridges inspired by owl wings

Cite as: Phys. Fluids **33**, 015123 (2021); <https://doi.org/10.1063/5.0035544>

Submitted: 30 October 2020 . Accepted: 30 December 2020 . Published Online: 29 January 2021

 Lei Wang (王雷),  Xiaomin Liu (刘小民), and  Dian Li (李典)



View Online



Export Citation



CrossMark

ARTICLES YOU MAY BE INTERESTED IN

[A study of the effect of serration shape and flexibility on trailing edge noise](#)

[Physics of Fluids](#) **32**, 127114 (2020); <https://doi.org/10.1063/5.0032774>

[Airfoil noise reductions through leading edge serrations](#)

[Physics of Fluids](#) **27**, 025109 (2015); <https://doi.org/10.1063/1.4907798>

[Aeroacoustic modal analysis of underexpanded pipe jets with and without an upstream cavity](#)

[Physics of Fluids](#) **33**, 016108 (2021); <https://doi.org/10.1063/5.0035133>

Physics of Fluids

SPECIAL TOPIC: Tribute to
Frank M. White on his 88th Anniversary

SUBMIT TODAY!

Noise reduction mechanism of airfoils with leading-edge serrations and surface ridges inspired by owl wings

Cite as: Phys. Fluids 33, 015123 (2021); doi: 10.1063/5.0035544

Submitted: 30 October 2020 • Accepted: 30 December 2020 •

Published Online: 29 January 2021



View Online



Export Citation



CrossMark

Lei Wang (王雷), Xiaomin Liu (刘小民), a) and Dian Li (李典)

AFFILIATIONS

School of Energy and Power Engineering, Xi'an Jiaotong University, Xi'an, Shaanxi 710049, People's Republic of China

^{a)}Author to whom correspondence should be addressed: liuxm@xjtu.edu.cn. Present address: Department of Fluid Machinery and Engineering, Xi'an Jiaotong University, 710049 Xi'an, China.

ABSTRACT

The remarkable characteristics of the silent flight of owls provide infinite inspiration for the low-noise operation of the rotating impeller machinery. However, how the characteristics of owl wings, including the leading-edge serrations, trailing-edge serrations, and plumed surfaces, affect the aerodynamic noise has not been studied comprehensively. According to previous research, the noise reduction level of an airfoil with an extensive sinusoidal profile is limited to a certain degree. In this paper, as a new coupling element, the surface ridge of owl wings is added to the airfoils with leading-edge serrations. Based on the NACA0012 (National Advisory Committee for Aeronautics) airfoil, the bionic airfoils with sinusoidal, serrated, and iron-shaped leading-edge serrations and surface ridges are reconstructed and studied to reveal the noise reduction mechanism of the coupled elements. The hybrid numerical method of large eddy simulation combined with the acoustic analog equations is adopted to predict the far-field acoustic characteristics. The vortex dynamic method is used to exposit the noise reduction mechanism of biomimetic flow control. The results demonstrate that the airfoil with iron-shaped leading-edge serrations has the best effect of noise reduction. Relative to the original airfoil, the sound pressure level is reduced by 14.3 dB. The change of streamwise vortices caused by the biomimetic structures leads the regular large-scale tubular vortices to separate into smaller horseshoe vortices. In addition, the correlation coefficient of spanwise is reduced, and the change of time-averaged vorticity in the space field promotes the attenuation effect of sound source caused by sound pressure fluctuation radiation.

Published under license by AIP Publishing. <https://doi.org/10.1063/5.0035544>

I. INTRODUCTION

With the rapid development of rotating machinery and its effect on the surrounding environment, noise hazards are increasingly receiving particularly strong complaints from nearby residents. Noise reduction remains an urgent problem to be solved.^{1–3} The current advanced design of a rotating turbine has taken noise as one of the important design indicators, and noise analysis and evaluation are directly incorporated into the wind turbine in the pneumatic design system simultaneously. The excellent flying ability and low-noise flying characteristics of birds provides continuous inspiration for the development of aerodynamic noise reduction technology. Through the studies of the wings and feathers of owls and eagles, Gramer⁴ found that the significant characteristics of silent flying by owls primarily involved the following three factors: comb-like

feathers at the leading-edge serrations, a velvet-like fluff on the wing surface, and fringe-like feathers at the trailing edge. Lilley⁵ noted that if we ignored the mechanism and technical research related to the noise suppression system of owls, we would miss a golden opportunity to design silent aircraft in the future. However, how these characteristics of wings affect the potential noise reduction functions still needed further exploration.⁶ Geyer^{7,8} studied the aeroacoustic characteristics of the real owl wing, finding that silent flight based on an owl's leading edge has considerable potential for application in new noise reduction technology.

Feinerman *et al.*⁹ measured the acoustic performance of a rotor blade with serrated leading-edge serrations and compared the experimental results of a traditional rotor blade with those of straight leading-edge serrations. It was found that the sound pressure level (SPL) of the blade with serrated leading-edge serrations in the main

radiation direction was reduced by 3 dB. Reboul *et al.*¹⁰ predicted the turbulent interference noise of the outlet guide blade of a fan with sinusoidal leading-edge serrations using the computational aeroacoustics method. The results showed that the overall sound power of the fan was reduced by ~2 dB, and the noise reduction level reached more than 4 dB at 2000 Hz. Lyu *et al.*¹¹ proposed a generalized Amite's model to predict the noise reduction effect of leading-edge serrations, and the validity of the prediction model was proved experimentally. This generalized model was more helpful for understanding the noise reduction mechanism of serrated leading-edge serrations and provided a theoretical reference for the design of new effective serrations. Kim *et al.*¹² used numerical simulation to study the noise reduction mechanism of the leading-edge protuberances. From the pressure fluctuation of the leading edge, it was found that the source cutoff effect caused by the geometric obliqueness reduced the sound pressure level radiation, and the phase interference between the peak and the trough center of the leading-edge structure helped to reduce the noise in the middle to high frequency ranges. Turner and Kim¹³ used a high-fidelity numerical simulation method for three-dimensional compressible Euler equations to compare the airfoils with smooth leading-edge serrations and sinusoidal leading-edge serrations and revealed the noise reduction mechanism of the vortex system of a sinusoidal structure. Clair *et al.*¹⁴ studied a type of passive flow control method based on sinusoidal leading-edge serrations that reduced the sound pressure level by 3 dB–4 dB without changing the aerodynamic performance. Narayanan *et al.*¹⁵ conducted an experimental study on the noise reduction effect of the isotropic homogeneous turbulence of sinusoidal leading-edge serrations. The results showed that the maximum noise reduction effect of the flat plates was 9 dB, and the noise reduction amplitude of the NACA-65 airfoil with leading-edge serrations was 7 dB. The above studies provided important theoretical references for the evolution and developmental details of the leading-edge vortices. Chen^{16–18} studied the influence of the leading-edge serrations on turbulent interference noise using a large eddy simulation (LES) and Ffowcs Williams–Hawkins (FW–H) acoustic analogy equation. The study indicated that the airfoil with sinusoidal leading-edge serrations had an obvious noise reduction effect in the middle to high frequency ranges, and the total sound pressure level at different square angles was reduced by 2.0 dB–5.5 dB. Tong *et al.*¹⁹ studied the influence of sinusoidal leading-edge serrations on the aerodynamic performance and interaction noise of turbine cascades. The results showed that the overall sound pressure level of turbulence interaction was reduced by 6 dB–8 dB. Paruchuri *et al.*²⁰ proposed three innovative leading-edge serrations, namely, double-sinusoidal serrations, chopped-peak serrations, and slotted-root serrations, and evaluated their aerodynamic and noise characteristics. It was found that a better noise reduction method is developed based on when the three biomimetic structures are used.

As we know, the silent flight of owls is the result of the cooperation of multiple function coupling elements. For owl wings, in addition to the leading-edge structure, the surface ridges are also an important function coupling element. However, the above studies primarily focus on the noise reduction ability and mechanism of the non-smooth leading edge of the airfoil. They do not consider the influence of surface ridges inspired by owl wings on the airfoil. The coupling effect of a non-smooth structure of the leading edge and surface ridge on the aerodynamic noise of the airfoil is not unclear.

In this study, to investigate the noise reduction ability and reveal the noise reduction mechanism of the multiple coupling elements inspired by owl wings, a biomimetic airfoil with non-smooth leading-edge coupled surface ridges is reconstructed first. The reference airfoil for the biomimetic design is the NACA0012 airfoil. The non-smooth structures of the leading edge include the sinusoidal, serrated, and innovative iron-shaped serrations. Then, the unsteady flow fields and sound fields around the biomimetic airfoils are solved using the hybrid numerical method of large eddy simulation (LES) combined with Ffowcs Williams–Hawkins (FW–H) acoustic analogy theory. Based on the numerical results, the swirling features of leading-edge vortices and spanwise correlations of the biomimetic airfoils are investigated. The vortex dynamic method is used to explore the noise reduction mechanisms of the biomimetic airfoils. The results show that the leading-edge serrations coupled with the surface ridges play an important role in the noise reduction and flow control of an airfoil. This study will provide a useful theoretical basis for the development of the design of aeroacoustic control.

II. NUMERICAL METHOD

In this study, the near-field flow obtained from the LES numerical simulation such as pressure pulsation and vortex shedding is used as the feeding date of the FW–H acoustic analog theory to predict the propagation of sound from its generation.^{16,21}

A. LES model

The LES method²² performs low pass filtering on the Navier–Stokes (N–S) equation and obtains a large-scale vortex and small-scale vortex after filtering. The large vortex generated by turbulent motion is solved by using N–S equations. The wale-adapting local eddy-viscosity (WALE) model²³ is used to solve the filtered small-scale eddies due to its good capacity of simulating the transient flow field caused by complex geometry.

The theoretical filter is applied to the exact solution of the continuous N–S equations to smooth it. The filtered variables are defined as follows:

$$\begin{aligned}\bar{u}(x, t) &= \int_{-\infty}^t \int_{-\infty}^{+\infty} G(\bar{\Delta}, \bar{\theta}, |x - x'|, t - t') u(x', t') dx' dt \\ &= G(\bar{\Delta}, \bar{\theta}) * u(x, t),\end{aligned}\quad (1)$$

where $G(\bar{\Delta}, \bar{\theta}, |x - x'|, t - t')$ is defined as the kernel of the filter. The parameter $\bar{\Delta}$ is the cutoff length, and $\bar{\theta}$ is the cutoff time. In order to preserve certain symmetries of the N–S equations, G must depend on the distance $|x - x'|$. The filtered part is solved by subgrid-scale model.

The Mach number studied in this article is 0.02, which is much less than 0.3, so the airflow can be regarded as an incompressible fluid. For incompressible flows, density is defined as a constant. After filtering the N–S equation through the filter function, the filtered transient Navier–Stokes equations involving the equations of continuity and the momentum are obtained,

$$\rho \frac{\partial \bar{v}_i}{\partial x_i} = 0, \quad (2)$$

$$\rho \frac{\partial \bar{v}_i}{\partial t} + \rho \frac{\partial}{\partial x_i} (\bar{v}_i \bar{v}_j) = -\frac{\partial \bar{P}}{\partial x_i} + \mu \nabla^2 \bar{v}_i - \frac{\partial \tau_{ij}}{\partial x_j}, \quad (3)$$

where the subgrid-scale tensor τ_{ij} reflects the effects of movement of small-scale eddies and is given by

$$\tau_{ij} = \rho \bar{v}_i \bar{v}_j - \rho \bar{v}_i \bar{v}_j. \quad (4)$$

The eddy-viscosity is supposed as follows:

$$\tau_{ij} - \frac{1}{3} \tau_{kk} \delta_{ij} = -2\mu_t \bar{S}_{ij}, \quad (5)$$

$$\bar{S}_{ij} = \frac{1}{2} \left(\frac{\partial \bar{U}_i}{\partial x_j} + \frac{\partial \bar{U}_j}{\partial x_i} \right), \quad (6)$$

where \bar{S}_{ij} reflects the strain rate tensor and μ_t denotes the turbulent eddy viscosity.

The WALE model is adopted to compute the eddy viscosity μ_t in this study and is defined as

$$\mu_t = \rho L_s^2 \frac{(S_{ij}^d S_{ij}^d)^{2/3}}{(\bar{S}_{ij} \bar{S}_{ij})^{5/2} + (S_{ij}^d S_{ij}^d)^{5/4}}, \quad (7)$$

$$L_s = \min(kd, C_w V^{1/3}), \quad (8)$$

$$S_{ij}^d = \frac{1}{2} (\bar{g}_{ij}^2 + \bar{g}_{ji}^2) - \frac{1}{3} \delta_{ij} \bar{g}_{kk}^2, \quad (9)$$

$$\bar{g}_{ij} = \partial \bar{u}_i / \partial x_j, \quad (10)$$

where the von Karman constant k is 0.4187, V is the elementary volume, L_s is the mixed length of the grid, C_w is the Smagorinsky constant, and the default value in the WALE subgrid model is 0.325.

B. The FW-H equation

Lighthill's analogy theory lays the foundation of aeroacoustics. The theory of aeroacoustics starts from the study of jet noise by Lighthill. In 1950, Lighthill proposed to transform the basic equation (N-S) of fluid mechanics. Taking the pulsating gas density as an independent variable, the left-hand side of the equation is the classical acoustic wave equation, and the right-hand side of the equation is the term for the sound source. The typical Lighthill equation is obtained as follows:

$$\frac{\partial^2 \rho'}{\partial t^2} - c_0^2 \frac{\partial^2 \rho'}{\partial x_i^2} = \frac{\partial^2 T_{ij}}{\partial x_i \partial x_j}, \quad (11)$$

$$T_{ij} = \rho v_i v_j + (p' - c_0^2 \rho') \delta_{ij} - \sigma_{ij}, \quad (12)$$

where T_{ij} is the Lighthill tensor. The term of $(p' - c_0^2 \rho') \delta_{ij}$ is ignored under the high Reynolds numbers, and the term of σ_{ij} is ignored under the conditions of isotropy. At the same time, the Green function G_0 is introduced,

$$G_0(t, x | \tau, y) = \frac{\delta(t - \tau - |x - y|)}{4\pi c_0^2 |x - y|}. \quad (13)$$

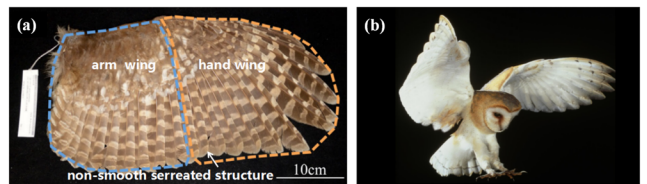


FIG. 1. (a) The detailed structure of an owl wing and (b) morphology of an owl.

The solution of this equation is

$$4\pi c_0^2 \rho'(x, t) = \frac{\partial^2}{\partial x_i \partial x_j} \iiint_V \left[\frac{T_{ij}}{|x - y|} \right] d^3 y. \quad (14)$$

On the right-hand side of the above equation is the quadrupole sound source. Based on the above theory, Curle considered the solid wall and further obtained the acoustic analogy equation as follows:

$$4\pi c_0^2 \rho'(x, t) = \frac{\partial^2}{\partial x_i \partial x_j} \iiint_V \left[\frac{T_{ij}}{|x - y|} \right] d^3 y + \frac{\partial}{\partial x_i} \iiint_{\partial V} \left[\frac{p' n_i}{|x - y|} \right] d^3 y. \quad (15)$$

On this basis, the solution of the far-field sound pressure is derived as follows:

$$p'(x, t) = \frac{x_i x_j}{4\pi |x|^2 c_0^2} \frac{d^2}{dt^2} \left\{ \iiint_V \frac{T_{ij}}{r} d^3 y \right\}_{t-r/c_0} - \frac{x_j}{4\pi |x| c_0} \frac{d}{dt} \left\{ \iint_{\partial V} \frac{p n_j}{r} d^2 y \right\}_{t-r/c_0}. \quad (16)$$

However, Curle did not consider the fluid vocalization of the interaction between the moving solid boundary and the fluid, which has certain limitations for the application of most rotating machinery. Later, Ffowcs Williams and Hawkings further considered the situation of the rotating wall and applied the generalized Green function method to the acoustic theory of Lighthill and Curle, which was extended to the problem of sound generation of fluids with arbitrary moving solid boundaries. The famous Ffowcs Williams–Hawkings (FW-H) equation is derived,

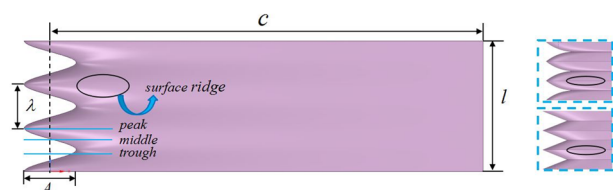


FIG. 2. Geometric models of different leading-edge serrations.

$$\frac{\partial^2(\rho'H)}{\partial t^2} - c_0^2 \frac{\partial^2(\rho'H)}{\partial x_i^2} = \frac{\partial^2}{\partial x_i \partial x_j} (T_{ij}H) - \frac{\partial}{\partial x_i} \left((p\delta_{ij} + \sigma_{ij}) \frac{\partial F}{\partial x_j} \delta(F) \right) + \frac{\partial}{\partial t} (\rho_0 V_n \delta(F)), \quad (17)$$

where $\delta(F)$ is a Dirac-delta function and H is a Heaviside function. The first term on the right-hand side of the equation is the quadrupole source caused by the volume integrals, which usually exists in a high-speed airflow. When the Mach number of the airflow is low, the quadrupole sound source may be neglected. The second term is the dipole sound source, which is affected by the pressure pulsation of the solid wall. The third item is the monopole sound source caused by the uneven mass and heat in the flow field, which is usually not considered in a stable physical field.

III. GEOMETRY MODEL AND BOUNDARY CONDITIONS

There are three geometric models in this study: sinusoidal, iron-shaped, and serrated leading-edge serrations. The average chord length is $c = 100$ mm, and the spanwise length is $l = 0.3c$. It is obviously observed that the shape of the nonsmooth edge of an owl wing is more similar to the iron-shaped distribution, as

shown in Fig. 1. The biomimetic airfoils are depicted in Fig. 2, including peaks, troughs, and surface ridges. To be specific, the ridges are the raised regions on the surface in addition to the leading edges. The wavelengths of biomimetic leading-edge serrations are $0.1c$ ($\lambda = 0.1c$), and the amplitudes are $0.12c$ ($A = 0.12c$).¹⁶ The average leading-edge baselines of the three leading-edge serrations coincide with the smooth airfoil so that the overall wetted areas basically remain constant. Additionally, taking the NACA0012 airfoil section as the reference section, the surface ridge structures are generated automatically by controlling the leading-edge curves when the scanning command is executed in the Pro/E software.

The leading-edge curves of the airfoils with sinusoidal leading-edge serrations, serrated leading-edge serrations, and iron-shaped leading-edge serrations are defined in the following equations:

$$c(z) = c + \frac{A}{2} \cos\left(\frac{2\pi}{\lambda} z\right) (0 \leq z \leq \lambda), \quad (18)$$

$$\begin{cases} c(z) = \frac{-2A}{\lambda} z + \frac{A}{2} \left(0 \leq z < \frac{\lambda}{2}\right), \\ c(z) = \frac{2A}{\lambda} z - \frac{3A}{2} \left(\frac{\lambda}{2} \leq z \leq \lambda\right), \end{cases} \quad (19)$$

$$\begin{cases} \left(c(z) + \frac{A}{2}\right)^2 = \frac{\lambda^2}{16} + \frac{A^4}{\lambda^2} + \frac{A^2}{2} - \left(z - \frac{\lambda}{4} + \frac{A^2}{\lambda}\right)^2 \left(0 \leq z < \frac{\lambda}{2}, \frac{-A}{2} \leq c(z) \leq \frac{A}{2}\right), \\ \left(c(z) + \frac{A}{2}\right)^2 = \frac{\lambda^2}{16} + \frac{A^4}{\lambda^2} + \frac{A^2}{2} - \left(z - \frac{3\lambda}{4} - \frac{A^2}{\lambda}\right)^2 \left(\frac{\lambda}{2} \leq z \leq \lambda, \frac{-A}{2} \leq c(z) \leq \frac{A}{2}\right), \end{cases} \quad (20)$$

where $c(z)$ is the distribution laws of the biomimetic leading-edge curves. The coordinates of the leading edge of the smooth airfoil are modified. The x -coordinate is stretched or compressed so that the chord lengths of the airfoils with biomimetic leading-edge serrations and the smooth airfoil are the same,

$$\begin{cases} x_2 = \begin{cases} \frac{x_1}{x_{max}} [x_{max} + (c(z) - c)] - [c(z) - c] (x_1 < x_{max}) \\ x_1 \end{cases} & (x_1 \geq x_{max},) \\ y_2 = y_1, \end{cases} \quad (21)$$

Equation (21) shows the parameters before and after the coordinate transformation in the x - and y -directions. The subscripts 1 and 2 refer to the pre- and post-transformation coordinates, respectively. The subscript max refers to the position of the maximum thickness. Additionally, y_1 and y_2 are the same in the coordinate transformation.

For convenient operation and implementation, the profile of the iron-shaped leading-edge serrations is described by a circular arc, and the circular arc segment at the trough is tangent to the straight line parallel to the x axis where the point is located, as shown in Fig. 3. A variable of the shape factor ψ is proposed to

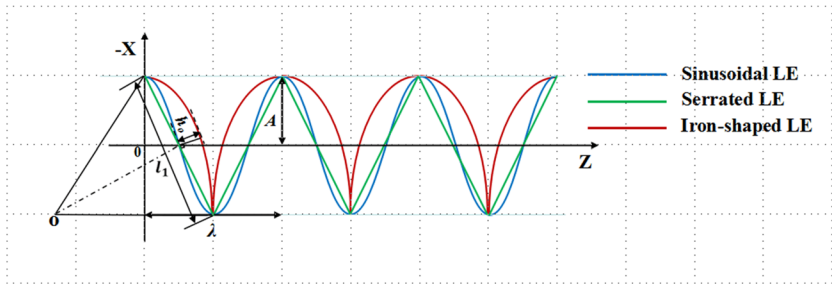


FIG. 3. Leading-edge curves of the three types of biomimetic leading-edge serrations.

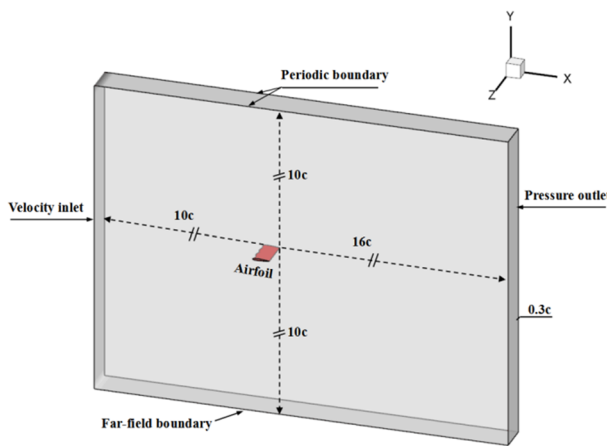


FIG. 4. Computational domain and boundary conditions.

further describe different biomimetic airfoils, as shown in the following equations:

$$\phi = \frac{\lambda}{2A}, \quad (22)$$

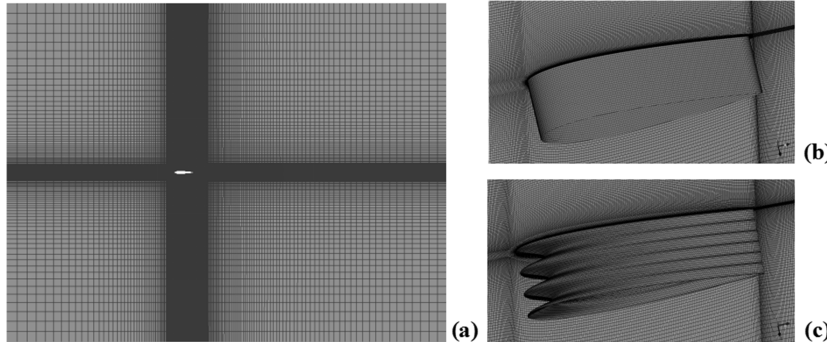


FIG. 5. Distributions of surface grids in detail: (a) grid distribution of the overall computational domain, (b) the surface grid of the smooth airfoil, and (c) the surface grid of the biomimetic airfoil.

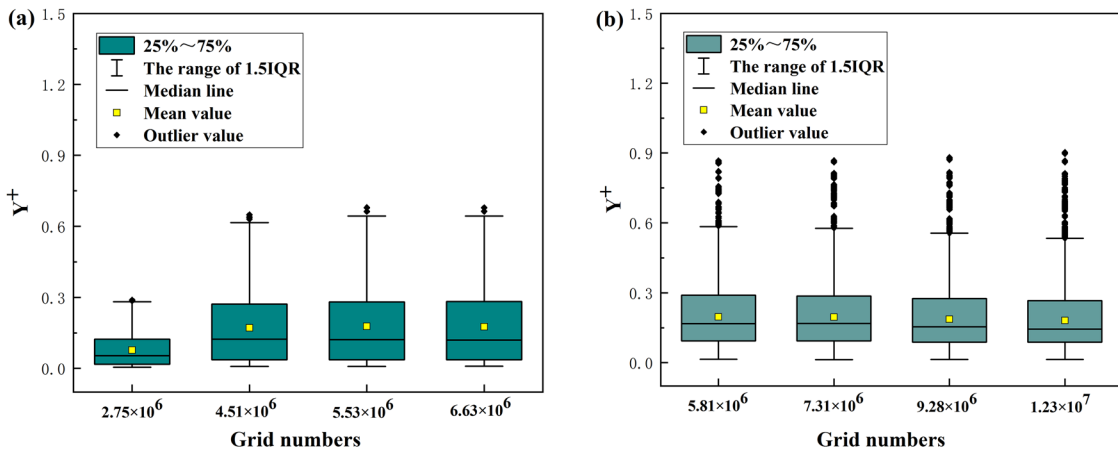
FIG. 6. The y^+ distributions of (a) the smooth airfoils and (b) the airfoils with sinusoidal leading-edge serrations with different mesh numbers.

TABLE I. Grid node distributions of the airfoils with sinusoidal leading-edge serrations.

Mesh	Grid amounts ($\times 10^4$)	Number of nodes (spanwise)	Number of nodes (chordwise)	Number of nodes (normal)
Coarser	581.55	103	343	148
Coarse	737.19	115	358	163
Moderate	927.89	127	378	178
Fine	1226.81	139	403	200

direction, $20c$ in the cross-stream direction, and $0.3c$ in the spanwise direction. The biomimetic leading-edge serrations with three cycles are exhibited in the spanwise direction. For the periodic boundary conditions, all physical quantities of the two walls are completely related after the corresponding constraints are imposed on the flow field.¹⁶

The Reynolds number is 4.8×10^4 based on the chord length of the smooth airfoil, which is roughly identical to the Reynolds number range for small rotating machinery. The velocity of the free flow is 7 m/s, and the angle of attack is 0° . The static pressure at the outlet is 101 325 Pa. The time step is set to 1×10^{-5} s in the numerical calculation, and the total physical time is 0.25 s. The commercial computational fluid dynamics software Ansys Fluent 18.0 is used

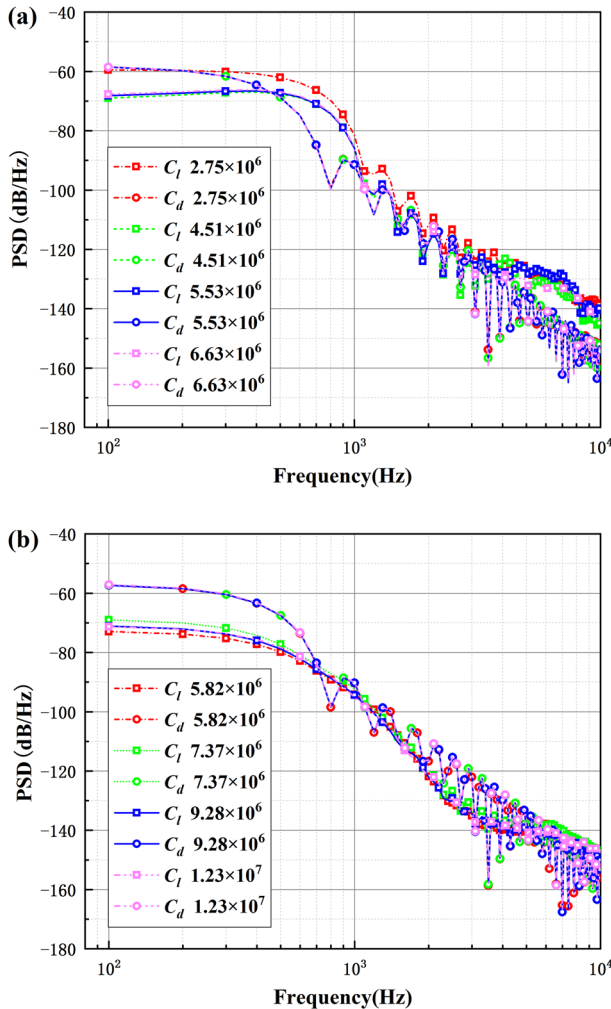


FIG. 7. The PSD distributions of the lift and drag coefficient of (a) the smooth airfoils and (b) the airfoils with sinusoidal leading-edge serrations of different mesh numbers.

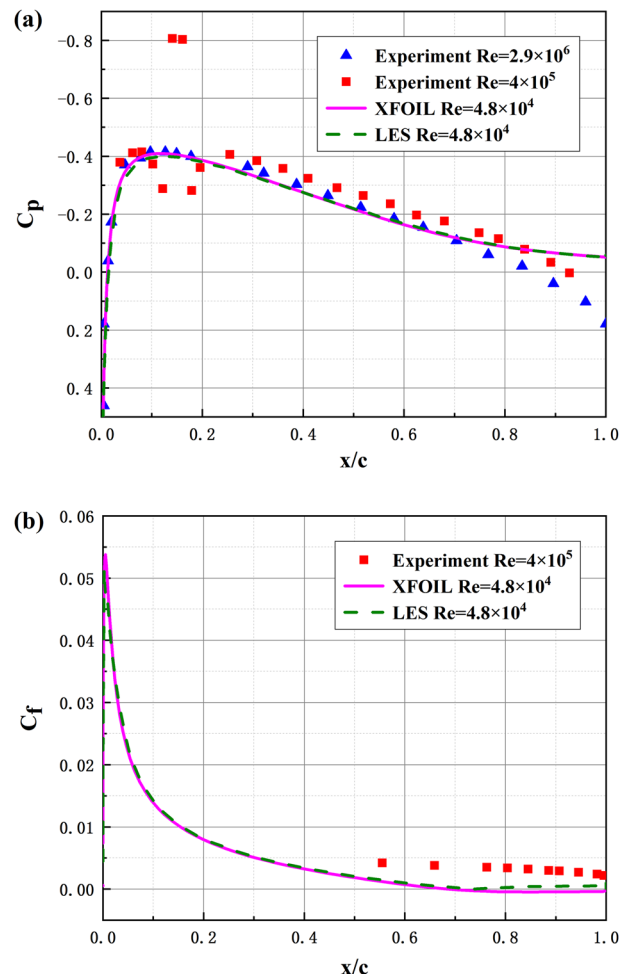


FIG. 8. The time-averaged C_p (a) and C_f (b) distributions of LES numerical simulation predictions ($Re_c = 4.8 \times 10^4$) compared with XFOIL simulations ($Re_c = 4.8 \times 10^4$) and experiments ($Re_c = 2.9 \times 10^6$ and $Re_c = 4 \times 10^5$).

for the numerical simulation. A finite volume method (FVM) was used to calculate the time-dependent turbulent flow based on the incompressible LES. The pressure–velocity coupling (SIMPLE) algorithm is adopted to solve the incompressible N-S equations. The time marching set as the second-order implicit scheme and convection and diffusion term set as the second order partial scheme and bounded central difference scheme are employed to reduce numerical dissipation. In detail, Gauss–Gauss node based gradient scheme is employed to solve the gradients of variables. The bounded central difference and second-order implicit scheme are adopted to discretize the momentum and transient formulation.

The surface grids of the smooth airfoil and the airfoil with biomimetic leading-edge serrations are shown in Fig. 5. Because of the similarity of the geometry structure, the mesh is divided according to the distribution of the airfoil with sinusoidal leading-edge serrations. The mesh nodes of three types of biomimetic structures stay the same in the x–y plane. The minimum mesh size at the tail of the airfoil is $0.88 \times 10^{-3} c$, and the average grid size along the flow direction of the biomimetic airfoils is $6.89 \times 10^{-3} c$, which is similar to that of the smooth airfoil. There are 320 grid nodes around the airfoil, and the grid element of the first layer meets the conditions $\Delta y^+ < 1$,^{24–26} $\Delta x^+ < 23$, $\Delta z^+ < 28$ (smooth leading-edge serrations), and $\Delta z^+ < 17$ ²⁷ (sinusoidal leading-edge serrations). Figure 6 shows the surface y^+ distributions of the smooth airfoil and the airfoil with sinusoidal leading-edge serrations, and the settings of specific grid nodes are shown in Table I. Considering the complexity of the airfoil with sinusoidal leading-edge serrations, the spanwise grids are increased and refined to reflect the true geometric and physical shape as much as possible.

The PSD distributions of the lift and drag coefficient of the airfoils are shown in Fig. 7, including the smooth airfoils and the airfoils with sinusoidal leading-edge serrations. The PSD distributions of the lift coefficient and drag coefficient are identical when the grid numbers of the smooth airfoils tend to 5.53×10^6 , and the grid numbers of the airfoils with sinusoidal leading-edge serrations are greater than 9.28×10^6 . Considering the trade-off between the calculation accuracy and the calculation time, a moderate mesh is adopted for further research in the end.

The smooth airfoil of NACA0012 is used for accuracy verification, and the results of the LES simulation are compared with XFOIL's results²⁸ and experiments in this paper. The distributions of the surface time-average pressure coefficient and skin friction coefficient are shown in Fig. 8, which shows that the agreement is good. In addition, the distributions of the surface pressure coefficients of other Reynolds numbers ($Re_c = 2.9 \times 10^6$, $Re_c = 4 \times 10^5$)^{29,30} are also shown in Fig. 8. The overall trend and distributions are similar. Furthermore, the velocity of the physical disturbance propagation must be less than the velocity of the solution of the time advancement. Besides, the Courant numbers of all investigated airfoils meets the CFL (Courant–Friedrichs–Lewy) condition that is necessary for the convergence requirement.³¹

IV. DISCUSSION OF RESULTS

As shown in Fig. 9, the PSD distributions of the lift coefficients show obvious differences, whereas the PSD distributions of the drag coefficients show good consistencies among the discussed airfoils.

Relative to the original airfoil, the attenuation of the lift coefficient of the airfoil with iron-shaped leading-edge serrations is the least and that of the airfoil with sinusoidal leading-edge serrations is the greatest. The changes in the lift coefficients have a slight influence on the aerodynamic performance at zero attack angle because of the symmetrical airfoils. In addition, the PSD distributions of the drag coefficients of the airfoils with three leading-edge serrations in the middle and low frequency regions are slightly higher than those of the original airfoil. The effect of the drag coefficients is negligible, in general, on the aerodynamic performance of the airfoils with biomimetic structures at zero attack angle.

The time-averaged pressure coefficient distributions of the smooth airfoil and the airfoils with three leading-edge serrations at different spanwise locations are shown in Fig. 10. The low-pressure regions are presented where the airflow at the trough of the leading-edge serrations enters, so it is easy to form larger adverse pressure

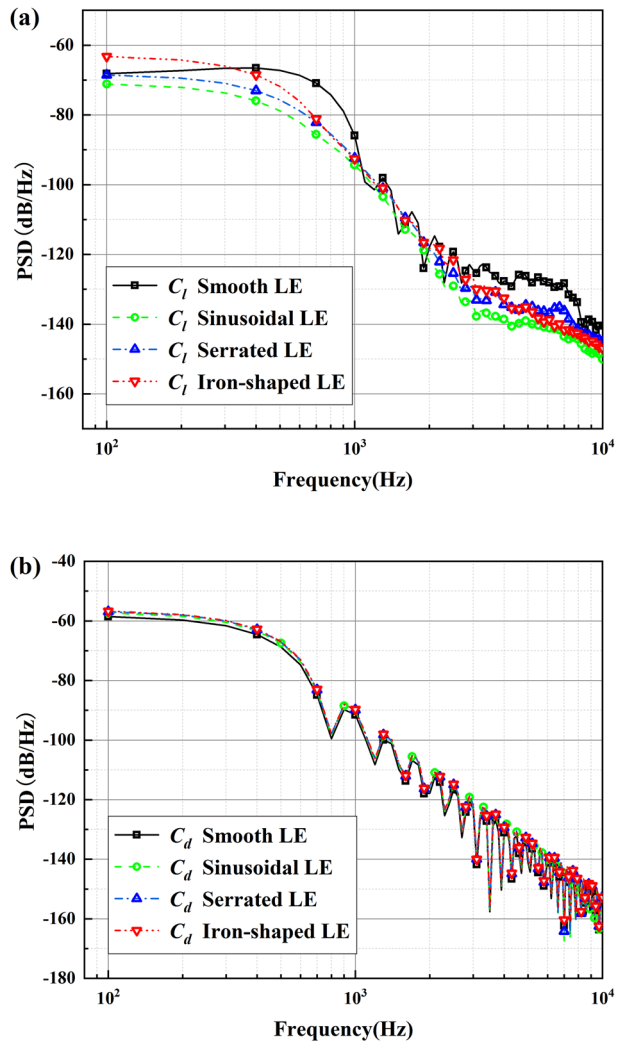


FIG. 9. The PSD distributions of the lift (a) and drag (b) coefficients of the smooth airfoils and the airfoils with different leading-edge serrations.

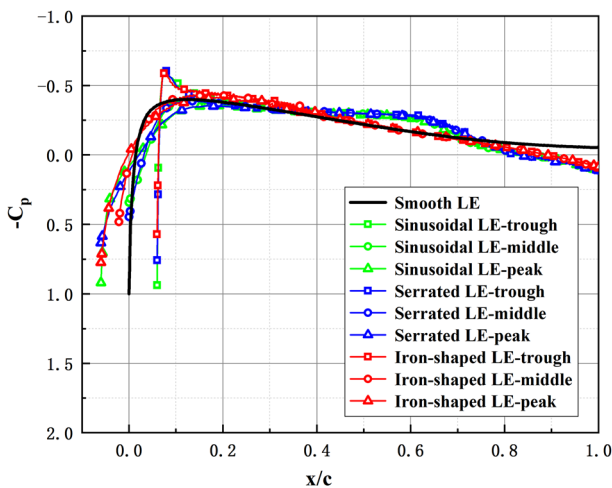


FIG. 10. The distributions of time-averaged pressure coefficients.

regions. The flow separations occur more easily in the adverse pressure regions. The pressure gradients in the spanwise direction are formed by the peak and trough section of the leading-edge serrations and cause secondary flows along the spanwise direction of the airfoils. The flow fields in the streamwise and spanwise directions are changed drastically, resulting in substantial differences in the pressure coefficients at the middle and rear parts of the biomimetic airfoils and the smooth airfoil. Compared with those of the other biomimetic airfoils, the time-averaged pressure coefficient distribution of the airfoil with iron-shaped leading-edge serrations shows a

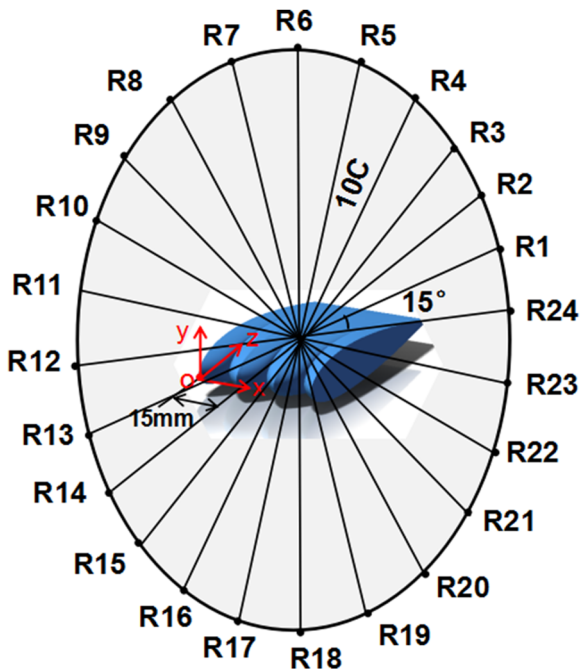


FIG. 11. Arrangement of sound source monitored points.

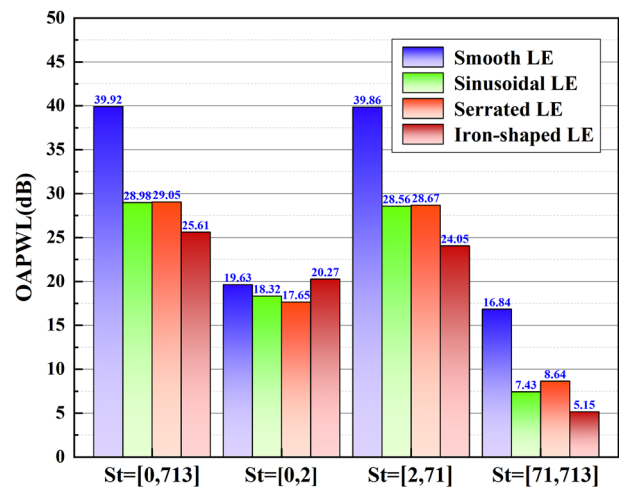
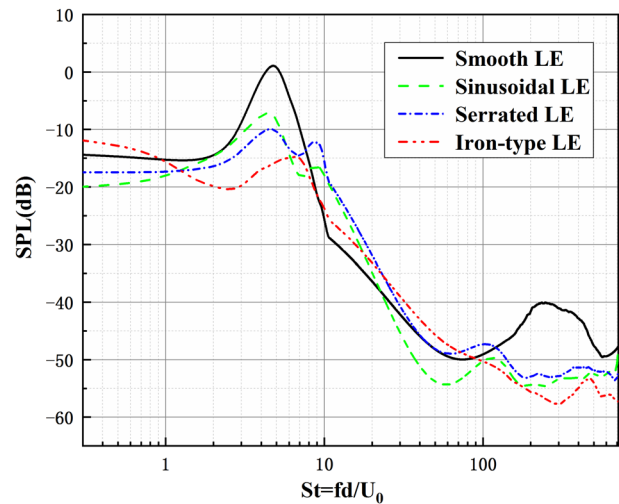
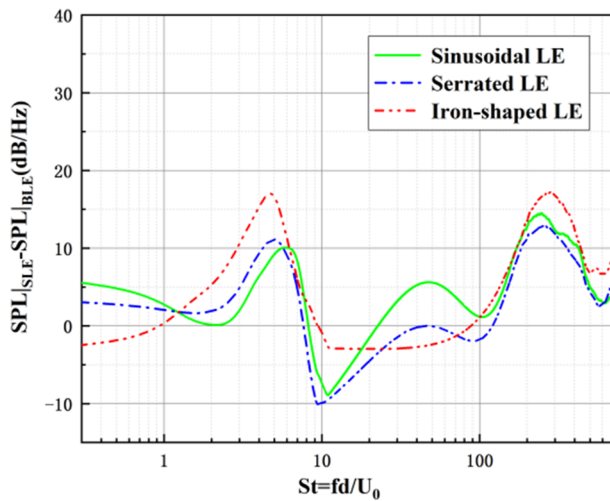


FIG. 12. Integration of OAPWLs in different frequency bands.

better consistency in the middle part of the smooth airfoil, and the flow separation points along the iron-shaped leading-edge serrations relatively move forward. The pressure coefficient distributions of the three biomimetic airfoils are similar at the trailing edges of the airfoils. The flow fields of the leading edges and trailing edges of the airfoils are changed. The monitored points around the airfoils are shown in Fig. 11.

The overall sound power level (OAPWL) integrated over different frequency ranges are further plotted in Fig. 12 to specifically assess the sound suppression of the biomimetic airfoils in different frequency bands. According to the division principle of low frequency, intermediate frequency, and high frequency, the selected frequency bands are set as $St = [0,2]$, $[2,71]$, and $[71,713]$. A clear noise reduction of 14.31 dB generated by the iron-shaped leading

FIG. 13. Distributions of sound pressure levels ($\theta = 90^\circ$).

FIG. 14. Sound pressure reduction levels ($\theta = 90^\circ$).

edge is attractive in the entire spectra, and the noise reduction effect of sinusoidal and serrated leading edge is equivalent. When the spectra are integrated over the frequency bands of $St = [2, 71]$ and $St = [71, 713]$, the OAPWL of the original airfoil is distinctly reduced by three biomimetic leading-edges. This implies that a large sound suppression generated by the biomimetic structure is noticeable in the mid to high frequency, which is similar to the result of the literature.³² Furthermore, as an effective passive noise reduction method, biomimetic flow control plays an important role in decreasing the airfoil self-noise.

The sound pressure level (SPL) and the sound reduction level are shown in Figs. 13 and 14 at the receiver located at $\theta = 90^\circ$, respectively. Similar to the OAPWL distribution over the entire spectra, the SPLs generated by the biomimetic airfoils in the mid-to-high frequency bands are decreased significantly compared with the prototype airfoil, and the airfoil with the iron-shaped leading edge has the maximum amplitude of noise reduction. Remarkably, the frequency band around $St = 5$ is obviously reduced of the original airfoil, and

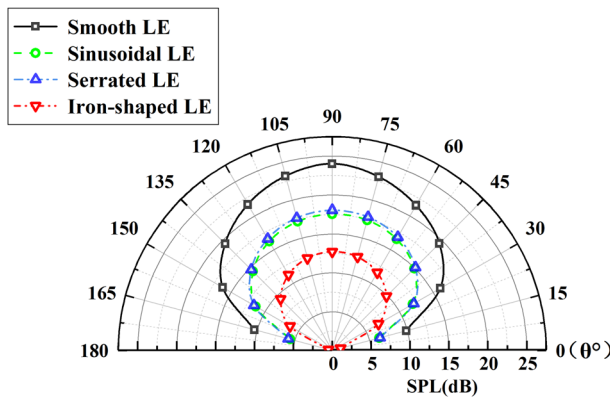


FIG. 15. Spatial distributions of sound pressure levels.

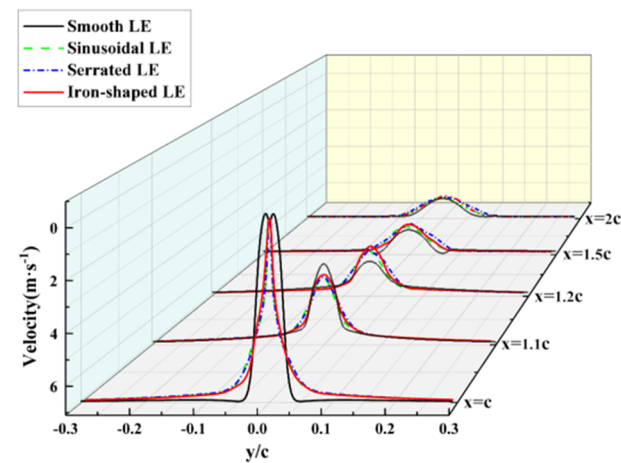


FIG. 16. Distributions of wake velocities along the streamwise direction.

the reduction level is up to 15 dB. However, the noise in some frequency bands is larger than the original airfoil, which is verified that it is caused by the increased discrete noise of vortex shedding. Due to the low Mach number, the dipole source dominates the contribution of the sound source. The SPL directivity distributions of the far field are depicted in Fig. 15. It is observed that the SPL directivity of biomimetic structures is unchanged, and the noise reduction level is similar in all directions.

To further describe the influence of the biomimetic leading-edge serrations on the aerodynamic performance of the airfoils at zero attack angle, the wake flow distributions of the airfoils are shown in Fig. 16. The wake velocity distributions are changed by biomimetic leading-edge serrations. The effects of the wake flows decrease as airflows move away from the tail of the airfoils. There are apparent differences in the velocities at the positions of $x = 1.1c$ and $x = 1.2c$. The wake velocities of the biomimetic airfoils increase along the downstream, which is in accordance with the results of Ref. 33.

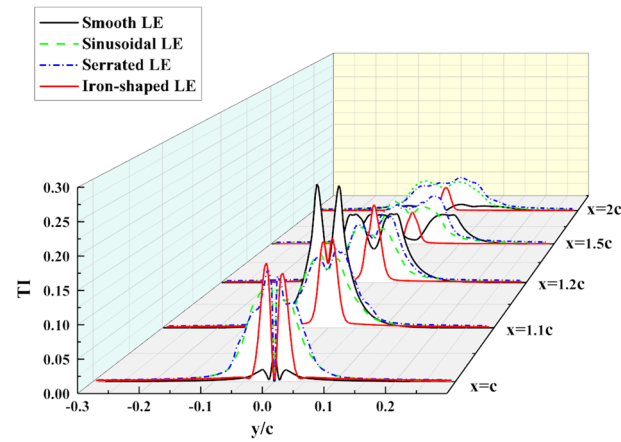


FIG. 17. Distributions of TIs along the streamwise direction.

The turbulent intensity reflects the intensity of turbulent fluctuation. The time-averaged TIs of the spatial points are monitored in the regions of downstream wakes. The TIs of the smooth airfoil and the biomimetic airfoils exhibit an obvious double-peak effect in the near wake regions from Fig. 17. The double-peak effect of the smooth airfoil increases first and then decreases with airflow away from the tail of the airfoil. Moreover, the biomimetic airfoils show gradual weakening attenuation trends that differ from those of the smooth airfoil. In particular, the double-peak effect of the airfoil with iron-shaped leading-edge serrations gradually attenuates as it moves away from the wake region and the crest values also gradually decrease. This indicates that the turbulent pulsation is gradually decreased. Furthermore, the TIs of the biomimetic airfoils at $x = 1.1c$ decay rapidly. After fully developing, a part of the energy of vortex shedding is dissipated and the TIs are weakened.

The momentum exchange generated by velocity fluctuations in the spanwise direction is minor, so Reynolds stress on the x-y plane plays a dominant role for all investigated airfoils. The Reynolds stress

distributions of the original airfoil and airfoils with three leading-edge serrations on the x-y plane are described in Fig. 18. To further reveal the influence of biomimetic leading-edge serrations on the stress distributions of the flow fields in the spanwise direction, the Reynolds stress distributions at the peak, trough and middle section are given. The stress distributions of all airfoils in the wake are symmetrical and reversely distributed. The Reynolds stress of the smooth airfoil is primarily distributed in the wake away from the airfoil. The airfoils with three types of biomimetic leading-edge serrations all change the positions of entire Reynolds stress distributions in the second half part of the airfoils. The crest values of the Reynolds stress are distributed in the troughs of the biomimetic leading-edge serrations, and the minimum values are distributed in the peaks of the biomimetic leading-edge serrations. The entire Reynolds stress distributions of the airfoils with the other leading-edge serrations are larger than those of the airfoil with an iron-shaped leading-edge serration. It is indicated that the turbulent energy of the airfoil with iron-shaped leading-edge serrations is minimum, and the energy

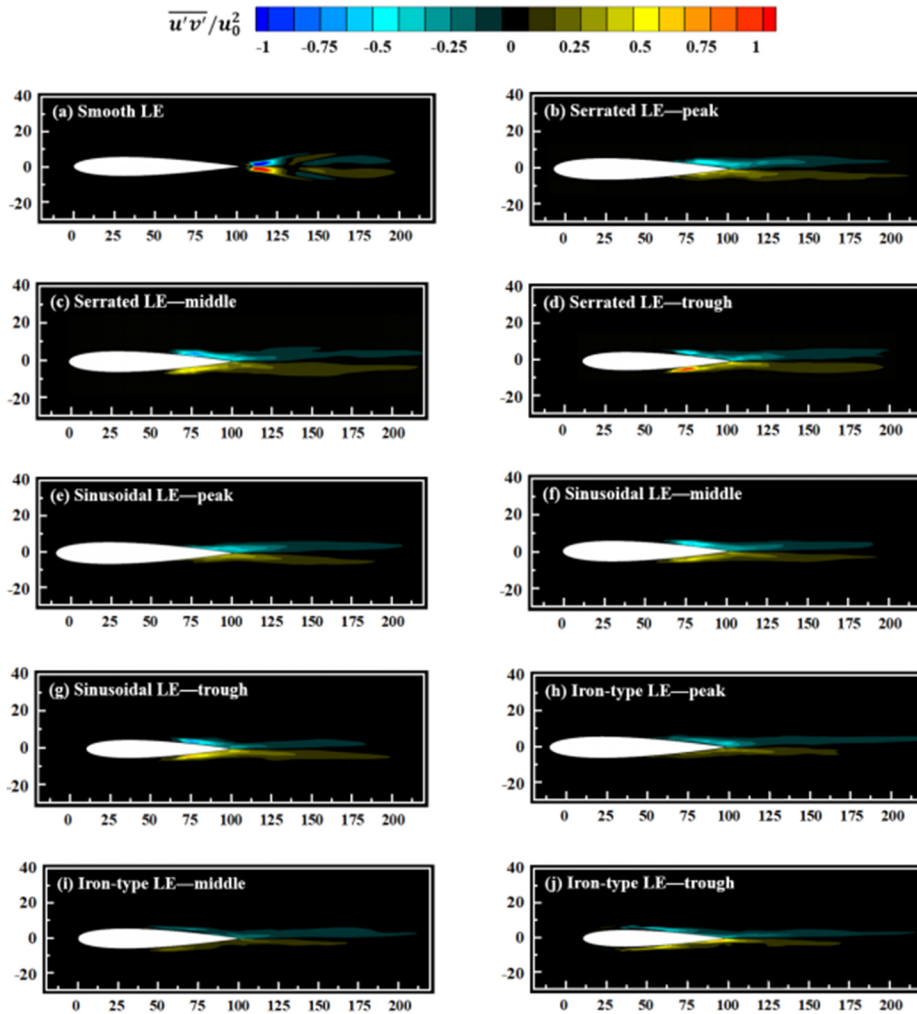


FIG. 18. Reynolds stress distributions of the smooth airfoil and airfoil with three biomimetic leading-edge serrations at different spanwise locations. (a) Smooth LE-peak, (b) serrated LE-peak, (c) serrated LE-middle, (d) serrated LE-trough, (e) sinusoidal LE-peak, (f) sinusoidal LE-middle, (g) sinusoidal LE-trough, (h) iron-shaped LE-peak, (i) iron-shaped LE-middle, and (j) iron-shaped LE-trough.

dissipation of the sound field in the process of expansion in the cross-stream direction is higher than the other two biomimetic airfoils. The Reynolds stress can reflect the intensity of turbulence to some extent. The distributions near the wake region of the airfoils correspond to the results of Fig. 19.

The generation and propagation of the sound source are closely related to the instantaneous pressure pulsation, and the pressure fluctuation can well reflect the turbulent noise in the flow field.^{34,35} In this paper, the time-averaged pressure fluctuation that is defined as Eq. (26) is introduced to evaluate the effect of different biomimetic leading-edge serrations on the source fields,

$$P'_{\text{rms}} = \sqrt{\text{var}(p'(z_1, t))} \quad (26)$$

where $p'(z_1, t)$ is the time-averaged transient pressure of the flow field at a certain point and var is the variance of transient pressure signals in a series of time. The P'_{rms} of the studied airfoils are depicted in Fig. 19. The range and magnitude of P'_{rms} correspond

to the noise reduction levels. The results show that the P'_{rms} in the middle and near wake region of the original airfoil are substantially improved by three biomimetic airfoils. The range and magnitude of Reynolds stress are weakened compared with the original airfoil. As a result, the overall distributions move forward. Similar to the vortex cloud chart described later, the range and magnitude of transient pressure fluctuations from the middle and rear parts of airfoils with sinusoidal and serrated leading-edge serrations gradually move forward from the wake region. The improvement of the airfoil with iron-shaped leading-edge serrations is remarkable, and the impact is gradually decreased along the downstream. Moreover, the transient pressure fluctuation of the airfoil with iron-shaped leading-edge serrations begins to develop from the leading-edge serrat part near the airfoil. Additionally, the peak scope and value of the pressure pulsation are smallest, which means that the energy generated by sound-field radiation is the least. Based on the above discussion, the airfoil with a biomimetic design is significant for further improving the noise reduction ability.

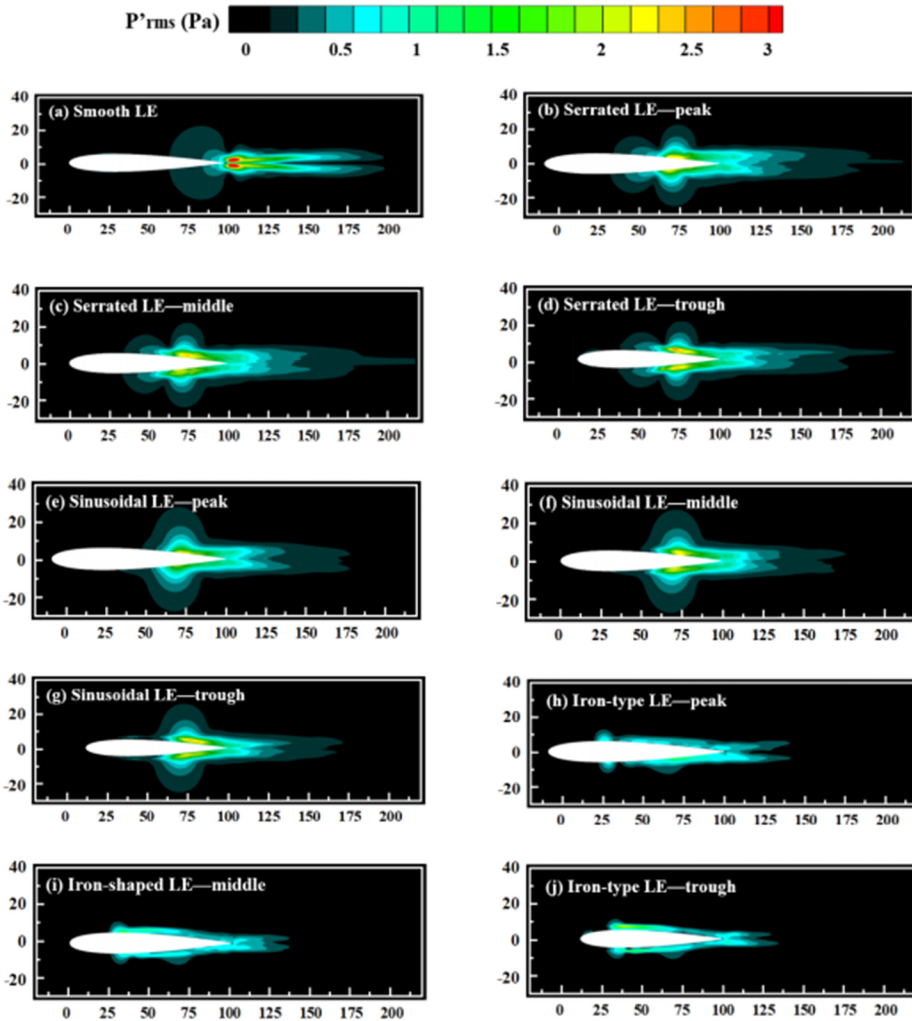


FIG. 19. Time-averaged pressure fluctuation distributions of the smooth airfoil and airfoil with three biomimetic leading-edge serrations at different spanwise locations. (a) Smooth LE-peak, (b) serrated LE-peak, (c) serrated LE-middle, (d) serrated LE-trough, (e) sinusoidal LE-peak, (f) sinusoidal LE-middle, (g) sinusoidal LE-trough, (h) iron-shaped LE-peak, (i) iron-shaped LE-middle, and (j) iron-shaped LE-trough.

The spanwise correlation length scale was proposed by the literature³⁶ to further evaluate the overall noise reduction level and amplitude. It is closely related to the evolution of the instantaneous vortices and has an important influence on the energy dissipation of the sound field. The literature^{16,35,37} also gave verifications separately.

The spanwise correlation is defined as

$$R_{pp}(\Delta z) = \frac{\overline{p'(z)p'(z + \Delta z)}}{p'^2} = \frac{\text{cov}(p(z_1, t), p(z_2, t))}{\sqrt{\text{var}((p(z_1, t))\text{var}(p(z_2, t))}}, \quad (27)$$

where $\{\cdot\}$ is the time average of the monitored variable, cov is the covariance of the pressure signals at two positions in the span, and var is the variance of a series of pressure signals at the monitored point over time. The layout of monitoring points at the leading edge for a smooth airfoil and an airfoil with sinusoidal leading-edge serrations is shown in Fig. 20. The spanwise correlation coefficients of the smooth airfoil and the other biomimetic airfoils are exhibited in Fig. 21.

The spanwise correlation coefficient is related to the evolution of the turbulent vortices and the physical size of eddies. It is a key parameter for evaluating local noise prediction and revealing the noise reduction mechanism. It can be clearly observed that the spanwise correlation coefficients located at the two limiting planes of the investigated airfoils is 1, which is caused by the periodic boundary conditions imposed on the boundary. The spanwise correlation coefficient of the original airfoil stays the same. This is because the cross section along the spanwise direction is identical and the incoming flow is free stream. The correlation coefficients of the three biomimetic airfoils show approximate periodic bimodal distributions, and the spanwise correlation coefficients of the two monitoring points near the peak is the minimal. Furthermore, the local noise-reduction level is affected by the cross-correlation coefficient. By comparing the three biomimetic airfoils, the overall correlation coefficient of the airfoil with the iron-shaped leading edge is the

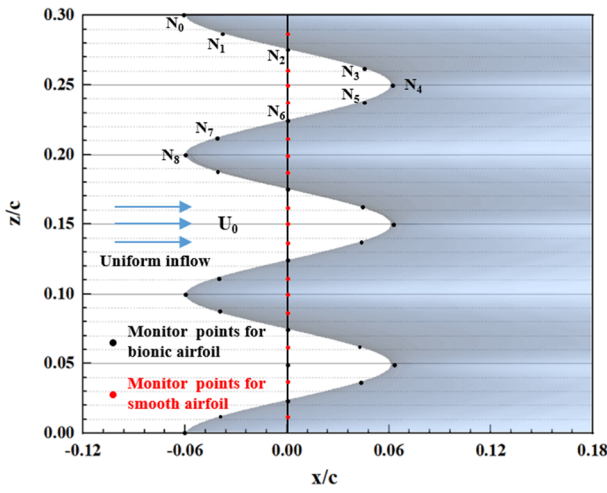


FIG. 20. Arrangement of leading-edge serrat monitoring points for the smooth airfoil and the airfoil with sinusoidal leading-edge serrat.

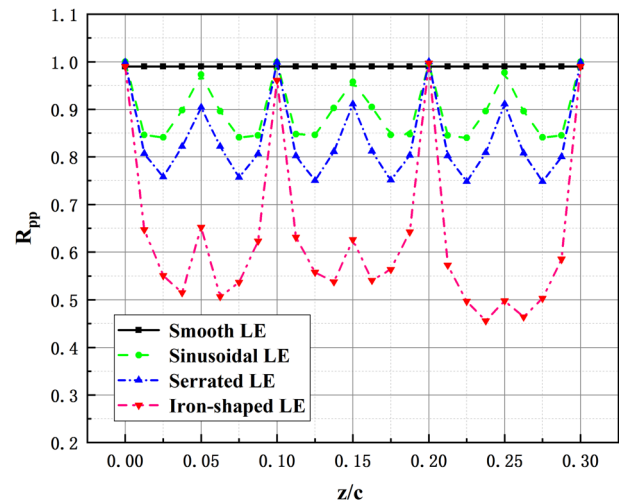


FIG. 21. Distributions of spanwise correlation coefficients of the smooth airfoil and the airfoil with biomimetic leading-edge serrations.

minimal, which indicates that the local noise radiation source of the iron-shaped leading edge maybe the least. Combining the vortex coherence structure behind, the biomimetic structure has a certain impact on the vortex structure of the downstream part of the airfoil through the change in the local correlation coefficient to reduce the overall sound pressure level.

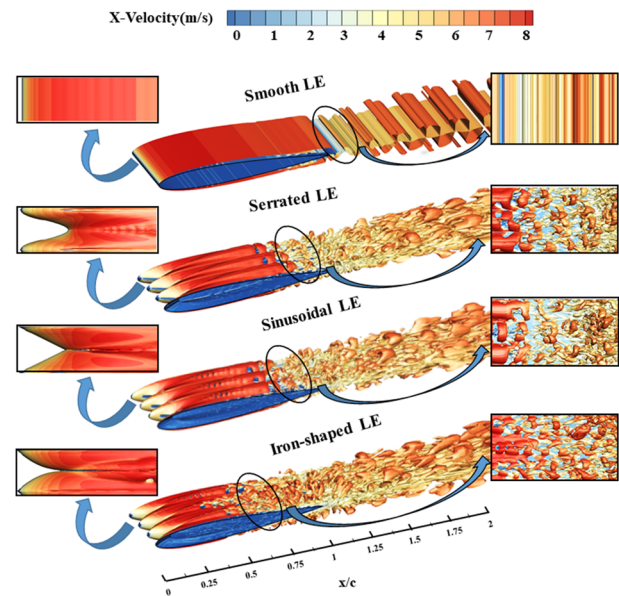


FIG. 22. Visualization of vorticity-velocity iso-surface distributions of the flow fields about smooth airfoil and the airfoils with biomimetic leading-edge serrations ($Q = 1000 \text{ s}^{-2}$).

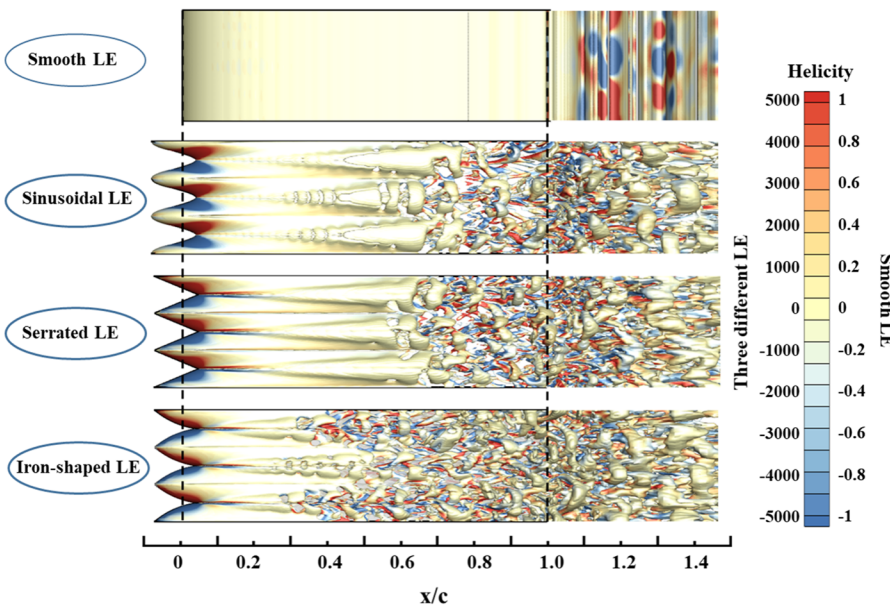


FIG. 23. Visualization of helicity–velocity iso-surface distributions of the flow fields about smooth airfoil and the airfoils with biomimetic leading-edge serrations ($Q = 1000 \text{ s}^{-2}$).

The coherent structures of vortex shedding play an important role in revealing the generation and development mechanism of noise. The Q criterion of the LES model can reflect the level of vorticity and the turbulence scale of the turbulence structure.³³ The Q -criterion is defined as

$$Q = \frac{1}{2} (\Omega_{ij}\Omega_{ij} - S_{ij}S_{ij}), \quad (28)$$

where Ω_{ij} and S_{ij} are the average tensor and average strain rate of the rotation speed, respectively. The value of Q is used to distinguish the rotational and nonrotational regions. High positive values indicate a region with low shear-strain rates and a high vorticity, otherwise,

the opposite.³⁸ The cloud charts of vorticity with $Q = 1000 \text{ s}^{-2}$ colored by velocity are selected to further reveal the evolution law of the vortices development energy of the flow boundary layer, as shown in Fig. 22. The vortices at the tail of the original airfoil present regular tube-shaped vortices, while the larger periodic tube-type vortices are detached and evolve into horseshoe-type vortices with smaller sizes using the biomimetic leading-edge serrations.

It is observed that the sizes of vortices generated by the boundary layer development of the three biomimetic airfoils are similar. After these periodic large-scale vortices are dissipated into small-scale vortices, the initial stability of the boundary layer is broken, which could have an effect on the acoustic feedback loop and overall noise reduction level. From the perspective of boundary layer

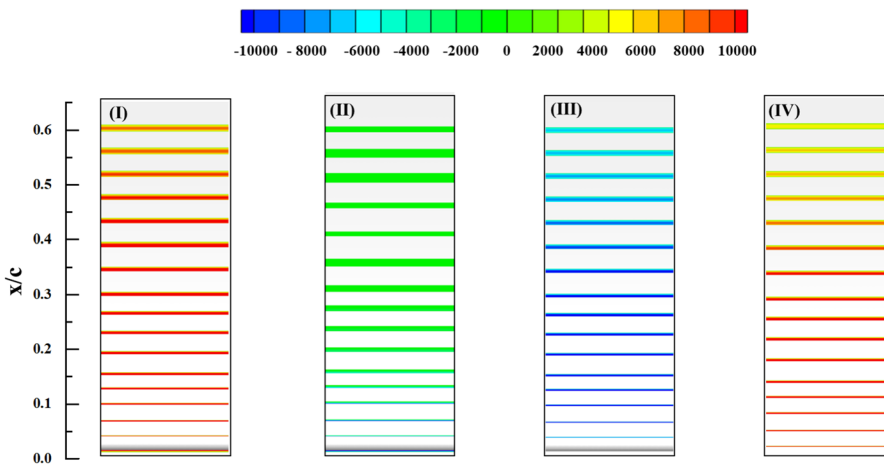


FIG. 24. Distribution of the time-averaged vorticity and its components of the smooth airfoil [(I) Time-averaged vorticity $|\bar{\omega}|$, (II) time-averaged vorticity $\bar{\omega}_x$, (III) time-averaged vorticity $\bar{\omega}_y$, and (IV) time-averaged vorticity $\bar{\omega}_z$].

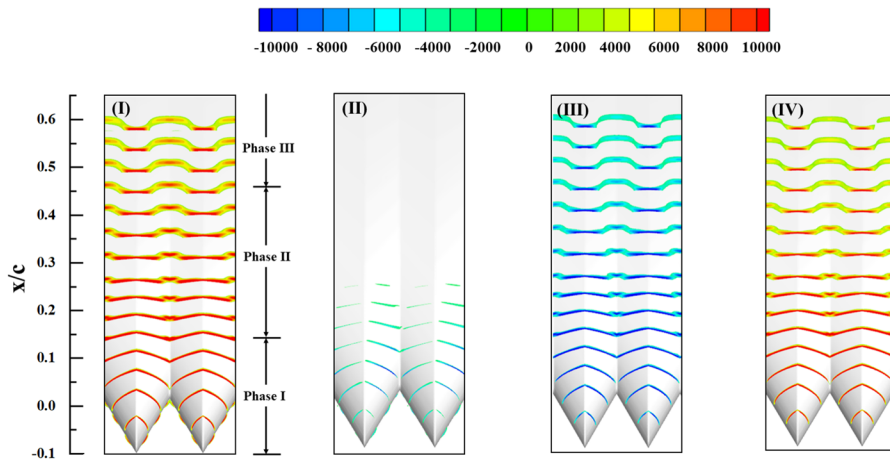


FIG. 25. Distribution of the time-averaged vorticity and its components of the airfoil with serrated leading-edge serrations [(I) Time-averaged vorticity $|\omega|$, (II) time-averaged vorticity $\bar{\omega}_x$, (III) time-averaged vorticity $\bar{\omega}_y$, and (IV) time-averaged vorticity $\bar{\omega}_z$].

development, the vortex coherent structure of the iron-shaped airfoil starts to develop in the midstream, and the number of small-scale vortices dissipated by large-scale vortices is more. Small-scale vortices play a dominant role in turbulent kinetic energy (TKE) dissipation due to molecular viscosity, so TKE dissipation generated by the airfoil with iron-shaped leading-edge serrations is the most, resulting in the minimal vortex shedding intensity. The boundary layer separation of the airfoils with serrated and sinusoidal leading-edge serrations is the latest, and the overall vortex shedding dissipates less radiation energy of the sound source, which results in a weaker noise reduction ability than that of the airfoil with an iron-shaped leading-edge serration. By observing the velocity distributions in the x -direction for the airfoil with biomimetic leading-edge serrations, it is apparent that the maximum velocities of the airfoils with serrated and sinusoidal leading-edge serrations are distributed on both sides of the downstream section of the trough. The maximum velocity of the airfoil with iron-shaped leading-edge serrations gathers at the same position of the trough, and the rapid increase in velocity leads to the development of a turbulent boundary layer. This

result is similar to the phenomenon of vortex shedding. In addition, vortices of the airfoil with iron-shaped leading-edge serrations fit better with the geometric model by observing the leading edge in detail, and the airfoil with serrated leading-edge serrations has the worst agreement. Additionally, the airfoil with iron-shaped leading-edge serrations has the largest energy dissipation of the leading edge.

To visualize the helical characteristics of the vortex shedding structure on the suction surface during the transition from laminar flow to turbulent flow, the spiral density³⁹ is described as the projection of the spin vector of the fluid in its momentum direction, which is defined as

$$h = \frac{\mathbf{U} \cdot \boldsymbol{\omega}}{|\mathbf{U}| |\boldsymbol{\omega}|}, \quad (29)$$

where \mathbf{U} denotes the velocity and $\boldsymbol{\omega}$ represents the vortical vector. A positive value of the helicity density means that the direction of rotation of the fluid is the same as the direction of velocity. On the

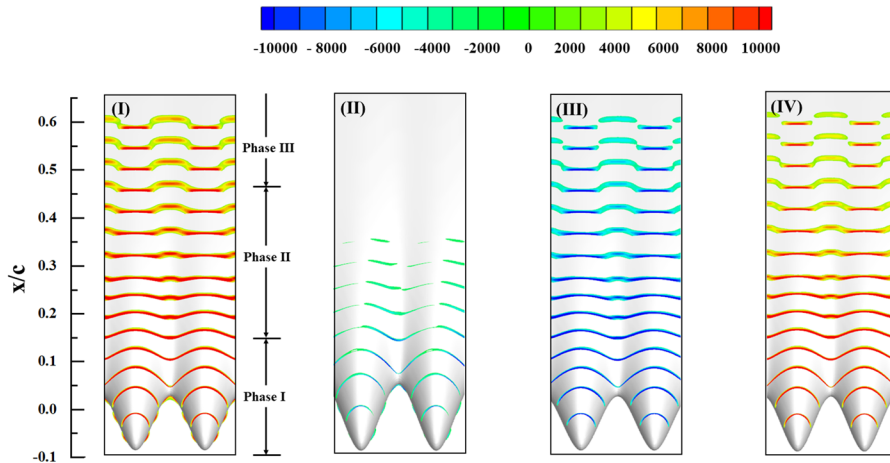


FIG. 26. Distribution of the time-averaged vorticity and its components of the airfoil with sinusoidal leading-edge serrations [(I) Time-averaged vorticity $|\omega|$, (II) time-averaged vorticity $\bar{\omega}_x$, (III) time-averaged vorticity $\bar{\omega}_y$, and (IV) time-averaged vorticity $\bar{\omega}_z$].

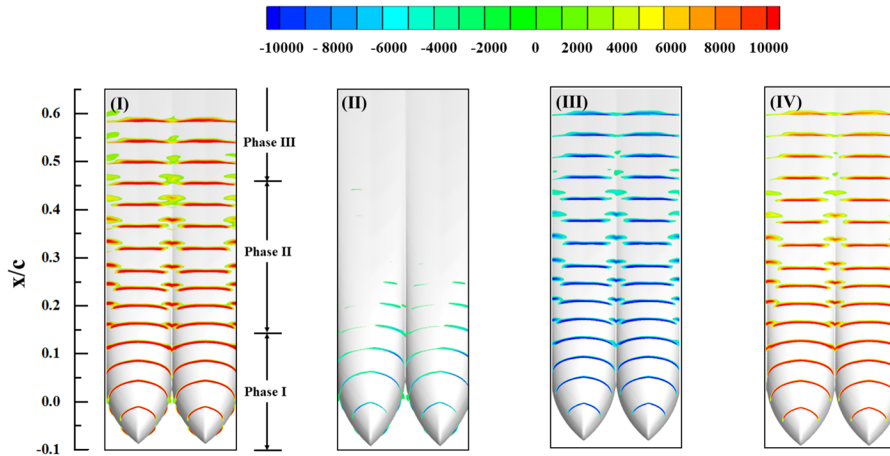


FIG. 27. Distribution of the time-averaged vorticity and its components of the airfoil with iron-shaped leading-edge serrations [(I) Time-averaged vorticity $|\omega|$, (II) time-averaged vorticity $\bar{\omega}_x$, (III) time-averaged vorticity $\bar{\omega}_y$, and (IV) time-averaged vorticity $\bar{\omega}_z$].

contrary, a negative value means that the direction of rotation of the fluid is opposite to the direction of velocity. The crest value of the helicity density of the original airfoil is much lower than those of the three biomimetic airfoils in Fig. 23. The helical characteristics of the wake vortex shedding are very intense when the airflows pass through the three types of biomimetic airfoils. When the airflows pass the spanwise symmetric structures of the biomimetic leading edges, the helicity densities present obvious symmetric characteristics of positive and negative values. The helical characteristic of the airfoil with sinusoidal leading-edge serrations evolves dramatically from the middle parts of the leading-edge serrations along the downstream direction, especially at the troughs. The helicity density of the airfoil with serrated leading-edge serrations is similar to that of the airfoil with sinusoidal leading-edge serration at a certain degree. The difference is that the development of the helical characteristic of the airfoil with iron-shaped leading-edge serrations is relatively slow. In addition, no obvious crest value aggregation effect weakens the impact of fluid on the trough of the leading edge. The developments of the helical characteristics of vortices along the downstream direction present the same evolution trend due to the ridge structures on the surfaces. At the leading edge, the vortex shedding energy dissipates in advance (Fig. 24).

To further understand the vortex distributions of the biomimetic airfoils, the time-averaged vortex distributions of the investigated airfoils, including their x-, y-, and z-components in three directions, are shown in Figs. 24–27. The vortex developments of the biomimetic airfoils are generally divided into three phases. The first phase of the vortex evolution is dominated by the longitudinal vortex and the spanwise vortex. The ring structures dominated by the ω_z component gradually appear in the second phase. The vortex rings of the ω_x component almost disappear in the third phase because of diffusion, which follows the evolution law described in the literature.⁴⁰

By observing the vortices of the smooth airfoil, it is apparent that the distributions of the vortex component in the three directions are similar, and no shear layer is in the spanwise direction at the leading edge. The vorticity of the prototype airfoil is gradually dissipated by using three biomimetic leading edge

along the downstream in the x-direction. The heart-shaped vortex rings of the airfoils with iron-shaped leading-edge serrations are conspicuous because of the large curvature at the transition of the trough. Apart from this result, the range and magnitude of vortex rings dissipate faster and are much lower than the other biomimetic airfoils in all directions. However, the ranges of vortex rings of the airfoils with serrated and sinusoidal leading-edge serrations are gradually enlarged along the downstream in the y- and z-directions. Therefore, the noise reduction capability of these two biomimetic airfoils is lower than the airfoil with iron-shaped leading-edge serrations. These findings indicate that the evolution energy of the vortices of the airfoil with iron-shaped leading-edge serrations is omnidirectionally lowered compared with the other airfoils.

V. CONCLUSION

In this study, a hybrid LES/FW-H method is adopted to investigate the acoustic characteristics of the biomimetic airfoils inspired by owl wings. The vortex dynamic method is used to analyze the self-noise reduction mechanism of the airfoils with different biomimetic leading-edge serrations. The main conclusions are summarized as follows:

- (1) On the premise of ensuring the aerodynamic performance of the airfoils, the biomimetic leading-edge serrations not only improve the peak scope and amplitude of the time-averaged sound pressure fluctuation of the original airfoil but also substantially attenuate the peak scope of the TI at the tail. The flow separation points of the biomimetic airfoils are advanced using the biomimetic leading-edge serrations. Moreover, the time-averaged pressure fluctuations and the TIs of the biomimetic airfoils are changed in variety at different locations.
- (2) The pressure fluctuation around the airfoil with iron-shaped leading-edge serrations is the least among the three types of biomimetic airfoils because of the design of this type of profile. The leading-edge design of the iron-shaped serrations

not only exerts the gentle influence of the sinusoidal leading-edge serrations on the airflow but also has the better channeling effect of the serrated serrations at the tail, which decreases the impact regions of local pressure. From the sound pressure levels of the monitored points, the noise reduction levels are equivalent when the shape factor ψ is 0 and are better when ψ is higher than 0. Therefore, it is worthwhile to further optimize the profile design of biomimetic leading-edge serrations.

- (3) Because of the application of the biomimetic leading-edge serrations, the tube-shaped vortices of the original airfoil are detached into horseshoe-type vortices with smaller sizes in the wake of the biomimetic airfoils. In addition, the radiation energy of the sound field dissipates gradually with the shedding of the horseshoe-type vortices. The energy dissipation of acoustic radiation is the highest when the vortex separation point of the airfoil with iron-shaped leading-edge serrations is advanced. Furthermore, the spanwise correlation coefficient of the original airfoil is reduced by the three types of biomimetic structures, which may be useful for exploring the more essential noise reduction mechanism.

ACKNOWLEDGMENTS

This work was supported by the National Key R & D Program of China (Grant No. 2019YFB1504600) and the National Natural Science Foundation of China (Grant No. 51676152).

DATA AVAILABILITY

The data that support the findings of this study are available from the corresponding author upon reasonable request.

REFERENCES

- ¹R. Camussi and G. J. Bennett, "Aeroacoustics research in Europe: The CEAS-ASC report on 2019 highlights," *J. Sound Vib.* **484**, 115540 (2020).
- ²D. Gély and G. J. Bennett, "Aeroacoustics research in Europe: The CEAS-ASC report on 2018 highlights," *J. Sound Vib.* **463**, 114950 (2019).
- ³E. WHO, *Environmental Noise Guidelines for the European Region* (World Health Organization Regional Office for Europe, Denmark, 2018), ISBN: 978 92 890 5356 3.
- ⁴R. R. Graham, "The silent flight of owls," *Aeronaut. J.* **38**, 837–843 (1934).
- ⁵G. M. Lilley, "A study of the silent flight of the owl," AIAA Paper 2009-2340, 2008.
- ⁶H. Wagner, M. Weger, M. Klaas, and W. Schröder, "Features of owl wings that promote silent flight," *Interface Focus* **7**, 20160078 (2017).
- ⁷T. F. Geyer, V. T. Claus, P. M. Hall, and E. Sarradj, "Silent owl flight: The effect of the leading edge comb," *Int. J. Aeroacoust.* **16**, 115–134 (2017).
- ⁸T. F. Geyer, E. Sarradj, and C. Fritzsche, "Silent owl flight: Acoustic wind tunnel measurements on prepared wings," AIAA Paper 2012-2230, 2012.
- ⁹J. A. Feinerman, S. Koushik, and F. H. Schmitz, "Effect of leading-edge serrations on helicopter blade-vortex interaction noise," *J. Am. Helicopter Soc.* **62**, 1–11 (2017).
- ¹⁰G. Reboul, A. Cader, C. Polacsek, T. L. Garrec, R. Barrier, and N. B. Nasr, "CAA prediction of rotor-stator interaction using synthetic turbulence: Application to a low-noise serrated OGV," AIAA Paper 2017-3714, 2017.
- ¹¹B. Lyu, M. Azarpeyvand, and S. Sinayoko, "Noise prediction for serrated leading-edges," AIAA Paper 2016-3714, 2016.
- ¹²J. W. Kim, S. Haeri, and P. F. Joseph, "On the reduction of aerofoil-turbulence interaction noise associated with wavy leading-edge serrations," *J. Fluid Mech.* **792**, 526–552 (2016).
- ¹³J. Turner and J. W. Kim, "Towards understanding aerofoils with wavy leading-edge serrations interacting with vortical disturbances," AIAA Paper 2016-2952, 2016.
- ¹⁴V. Clair, C. Polacsek, T. Le Garrec, G. Reboul, M. Gruber, and P. Joseph, "Experimental and numerical investigation of turbulence-airfoil noise reduction using wavy edges," *AIAA J.* **51**, 2695–2713 (2013).
- ¹⁵S. Narayanan, P. Chaitanya, S. Haeri, P. Joseph, J. W. Kim, and C. Polacsek, "Airfoil noise reductions through leading edge serrations," *Phys. Fluids* **27**, 025109 (2015).
- ¹⁶W. Chen, W. Qiao, F. Tong, L. Wang, and X. Wang, "Numerical investigation of wavy leading-edge serrations on rod-airfoil interaction noise," *AIAA J.* **56**, 2553–2567 (2018).
- ¹⁷W. Chen, W. Qiao, L. Wang, F. Tong, and X. Wang, "Rod-airfoil interaction noise reduction using leading-edge serrations," AIAA Paper 2015-3264, 2015.
- ¹⁸W. Chen, W. Qiao, X. Wang, L. Wang, and F. Tong, "An experimental and numerical investigation of airfoil instability noise with leading-edge serrations," AIAA Paper 2016-2956, 2016.
- ¹⁹F. Tong, W. Qiao, K. Xu, L. Wang, W. Chen, and X. Wang, "On the study of wavy leading-edge vanes to achieve low fan interaction noise," *J. Sound Vib.* **419**, 200–226 (2018).
- ²⁰C. C. Paruchuri, S. Narayanan, P. Joseph, and J. W. Kim, "Leading-edge serrations serratgeometries for significantly enhanced leading-edge serrations noise reductions," AIAA Paper 2016-2736, 2016.
- ²¹ANSYS Fluent: Theory Guide, Release 16.0, ANSYS, Inc., Canonsburg, PA, 2015, pp. 40–41.
- ²²Y. Jin, "Parameter extension simulation of turbulent flows," *Phys. Fluids* **31**, 125102 (2019).
- ²³F. Nicoud and F. Ducros, "Subgrid-scale stress modeling based on the square of the velocity gradient tensor," *Flow, Turbul. Combust.* **62**, 183–200 (1999).
- ²⁴T. Boulkeria, A. Ghenaiet, S. Mendez, and B. Mohammadi, "A numerical optimization chain combining computational fluid dynamics and surrogate analysis for the aerodynamic design of airfoils," *J. Aerosp. Eng.* **228**, 1964–1981 (2014).
- ²⁵M. Wang and X. Liu, "Numerical investigation of aerodynamic and acoustic characteristics of bionic airfoils inspired by bird wing," *Proc. Inst. Mech. Eng., Part G* **233**, 4004–4016 (2019).
- ²⁶M. Saniei and R. Razaghi, "Numerical investigation of three turbulence simulation models for S809 wind turbine airfoil," *Proc. Inst. Mech. Eng., Part A* **232**, 1037–1048 (2018).
- ²⁷W. Claus and H. Thomas, *Large-Eddy Simulation for Acoustics* (Cambridge University Press, 2007).
- ²⁸M. Drela, "XFOIL: An analysis and design system for low Reynolds number airfoils," in *Conference on Low Reynolds Number Airfoil Aerodynamics* (University of Notre Dame, 1989).
- ²⁹A. Bodling and A. Sharma, "Numerical investigation of noise reduction mechanisms in a bio-inspired airfoil," *J. Sound Vib.* **453**, 314–327 (2019).
- ³⁰A. Garcia-Sagrado and T. Hynes, "Wall pressure sources near an airfoil trailing edge under turbulent boundary layers," *J. Fluids Struct.* **30**, 3–34 (2012).
- ³¹L. Zhu, P. Wang, and Z. Guo, "Performance evaluation of the general characteristics based off-lattice Boltzmann scheme and DUGKS for low speed continuum flows," *J. Comput. Phys.* **333**, 227–246 (2017).
- ³²A. Corsini, G. Delibra, and A. G. Sheard, "The application of sinusoidal blade-leading edges in a fan-design methodology to improve stall resistance," *Proc. Inst. Mech. Eng., Part G* **228**, 255–271 (2014).
- ³³X. Liu, H. K. Jawahar, M. Azarpeyvand, and R. Theunissen, "Aerodynamic and aeroacoustic performance of serrated airfoils," AIAA Paper 2015-2201, 2015.
- ³⁴D. Li, X. Liu, F. Hu, and L. Wang, "Effect of trailing-edge serrations on noise reduction in a coupled bionic aerofoil inspired by barn owls," *Bioinspir. Biomim.* **15**, 016009 (2019).
- ³⁵F. Tong, W. Qiao, W. Chen, H. Cheng, R. Wei, and X. Wang, "Numerical analysis of broadband noise reduction with wavy leading-edge serrations," *Chin. J. Aeronaut.* **31**, 1489–1505 (2018).

- ³⁶S. Haeri, J. W. Kim, S. Narayanan, and P. Joseph, “3D calculations of aerofoil-turbulence interaction noise and the effect of wavy leading-edge serrations,” AIAA Paper 2014-2325, 2014.
- ³⁷A. Grébert, J. Bodart, and L. Joly, “Investigation of wall-pressure fluctuations characteristics on a NACA0012 airfoil with blunt trailing edge,” AIAA Paper 2016-2811, 2016.
- ³⁸I. Solís-Gallego, A. Meana-Fernández, J. M. Fernández Oro, K. M. Argüelles Díaz, and S. Velarde-Suárez, “LES-based numerical prediction of the trailing edge noise in a small wind turbine airfoil at different angles of attack,” *Renewable Energy* **120**, 241–254 (2018).
- ³⁹C. Rao, T. Ikeda, T. Nakata, and H. Liu, “Owl-inspired leading-edge serrations play a crucial role in aerodynamic force production and sound suppression,” *Bioinspir. Biomim.* **12**, 046008 (2017).
- ⁴⁰M. Zhao, M. Zhang, and J. Xu, “Flow physics behind the effects of leading-edge protuberances on the airfoil aerodynamic performance,” *J. Phys.: Conf. Ser.* **1037**, 022035 (2018).